

Accurate modelling of the crush behaviour of thin tubular columns using material point method

YANG PengFei^{1**}, MEGUID S. A.² & ZHANG Xiong^{1*}

¹ School of Aerospace, Tsinghua University, Beijing 10008, China;

² Mechanics and Aerospace Design Laboratory, University of Toronto, Toronto, ON, M5S 3G8, Canada

Received June 30, 2012; accepted November 23, 2012

In this paper, we apply the material point method (MPM), also known as a meshfree method, to examine the crush behaviour of thin tubular columns. Unlike the finite element method, randomly-distributed-weak-particle triggers were used to account for the deformation behaviour of collapse modes. Both symmetric and asymmetric modes of deformation and their associated mean collapse loads are determined for an elasto-plastic constitutive law describing the tubular columns. Attention was devoted to the accuracy and the convergence of the MPM simulation, which is determined by the number of the particles and the size of the background cells used in our explicit solver. Furthermore, a novel contact approach was adopted to establish the crush behaviour of the tubular columns. Two aspects of the work were accordingly examined, including three different crush velocities (5, 10 and 15 m/s) and varied geometrical features of the tube (t/d and l/d) based on the deformation history. The results of our model, which were compared with existing analytical predictions and experimental findings, identify the critical geometric features of the tubular columns that would dictate the deformation mode as being either progressive collapse or following Euler's buckling mode.

thin tubular columns, crush, material point method, deformation mode, elasto-plastic, mean collapse load

PACS number(s): 46.05.+b, 46.15.-x, 46.35.+z

Citation: Yang P F, Meguid S A, Zhang X. Accurate modelling of the crush behaviour of thin tubular columns using material point method. *Sci China-Phys Mech Astron*, 2013, 56: 1–11, doi: 10.1007/s11433-013-5073-x

1 Introduction

Thin wall tubular columns, particularly those of square or circular cross-section, subjected to axial crushing generally deform by progressive folding and thus possess favourable energy absorption characteristics. Because of their structural efficiency, versatility and low cost, they are extensively used in aerospace, automotive and civil engineering applications as energy absorbing barriers and arresters. They are characterized by limited magnitude of crippling force, large plastic deformation at a constant crush load and repeatable

mode of collapse.

The observations concerning the modes of collapse of tubular columns were first examined by Mallock [1]. Subsequently, Alexander [2] developed the first analytical expression of the quasistatic axial collapse of thin-walled cylindrical columns. He assumed a concertina mode in which the tubes fold up by forming axisymmetric rings. Pugsley et al. [3,4] later studied tubular columns with smaller wall thickness and developed the mean axial crushing load for the resulting diamond mode. By introducing curvature in the deforming fold length, Abramowicz and Jones et al. [5, 6] modified Alexander's model and examined the quasistatic and dynamic axial compression of cylindrical and square tubes. Johnson et al. [7] developed an expression for the

*Corresponding author (email: xzhang@tsinghua.edu.cn)

** Currently, on study leave from Mechanics and Aerospace Design Laboratory, University of Toronto, Toronto, ON, M5S 3G8, Canada

mean post buckling stress for the collapse of thin walled tubes using rigid-perfectly plastic material mode. Other researchers [8] classified the axial collapse of cylindrical tubes under quasi-static loading and presented a design chart which can predict the collapse mode for aluminium alloy tubes as a function of wall thickness-to-diameter ratio t/d and length-to-diameter ratio l/d . In addition, Singace et al. [9] examined the interplay of the factors influencing the different collapse modes in axially crushed tubes.

The finite element method (FEM) has also been widely used to study the collapse of thin wall tubes [10–16]. Rust et al. [10] discussed the circumstances under which the quasi-static limit load analysis could be performed by a transient analysis using explicit time integration scheme. They suggested that a quasi-static finite element analysis for multiple highly nonlinear crushing systems could be an advantageous alternative to implicit analysis. Arbitrary contact surfaces and status change in contact may cause convergence difficulties for implicit analysis. Marzbanrad et al. [11] studied the effects of the triggering of circular aluminium tubes on crashworthiness using explicit finite element method. Meguid et al. [12,13] carried out three-dimensional non-linear finite element analysis for quasi-static and dynamic collapse of square aluminium columns. Furthermore, Zhang et al. [14] introduced patterns to the surface of conventional thin-walled square tubes to improve the energy absorption capacity with the help of nonlinear explicit finite element analysis. Younes [15] used an explicit FEM to study the effect of varying configurations of the tube cross-section on the deformation response. Recently, Fyllingen et al. [16] compared the results modelled by shell elements and solid elements and suggested that shell elements with thickness stretch could be considered a good compromise for modelling thin wall tubes.

In spite of its widespread usage, the accuracy of the FEM relies on the contact algorithms adopted. Most contact algorithms are inconsistent because they rely heavily on contact elements that make use of penalty parameters which typically result in interpenetration between the impacting bodies. In the case of Lagrange multipliers, the solution is limited to frictionless contact and the resulting asymmetric stiffness matrix requires the use of special solvers. Furthermore, the presence of elements that are severely deformed will lead to inaccurate Jacobian matrix thus leading to erroneous results. The use of adaptive meshing to overcome highly distorted elements would ultimately lead to costly preprocessing. In addition, the reduction in element size using adaptive meshing could result in solution rounding off errors.

Several results have also been published on thin wall structure modelling using meshfree or element-free methods. Element-free Galerkin method has been employed with bi-cubic and quartic basis functions for shell and spatial structures [17]. Li et al. [18] presented a formulation based on the reproducing kernel particle method to study the large deformation behaviour of thin shells. Gato [19] also devel-

oped a meshfree method for fracture of thin-walled shells. In this paper, we apply a direct 3-D meshfree method to accurately study the crush behaviour of thin tubular columns.

In this paper, we present a novel approach which is based on explicit MPM solver to study the collapse of circular thin wall structures. MPM is suitable for treating problems involving large deformation accurately and efficiently [20]. MPM modelling does not involve element distortion as evident in FEM. Compared to the continuum shell theory approach, both the formulation and implementation of our proposed model are simpler and more consistent. Moreover, it is expected to yield more accurate predictions for the crush behaviour of tubular structures.

2 Description of material point method

2.1 Fundamentals of material point model

Material point method combines the description of Lagrangian particles and Eulerian background mesh, as illustrated in Figure 1. In the solution phase of MPM, particles are rigidly attached to the background grid and they deform with the grid. The momentum equation can be solved in the framework of standard finite element method. The positions and velocities of particles are updated by mapping back the obtained kinematic solution onto the grid nodes. The deformed grid is discarded in the subsequent time step and a new regular grid is used to avoid mesh distortion. For continuum domain, the mass conservation equation is given as:

$$\frac{d\rho}{dt} + \rho \nabla \cdot \mathbf{v} = 0. \quad (1)$$

The deformation of material is governed by the momentum equilibrium equation, such that

$$\nabla \cdot \boldsymbol{\sigma} + \rho \mathbf{b} = \rho \mathbf{a}, \quad (2)$$

where ρ is current density, $\boldsymbol{\sigma}$ is Cauchy stress, \mathbf{b} is body force per unit mass, and \mathbf{a} is the acceleration.

The weak form of eq. (2) can be obtained through weighted residual approach as being [21]

$$\int_{\Omega} \rho \mathbf{a} \cdot \delta \mathbf{v} d\Omega + \int_{\Omega} \rho \boldsymbol{\sigma}^s : \nabla \delta \mathbf{v} d\Omega - \int_{\Omega} \rho \mathbf{b} \cdot \delta \mathbf{v} d\Omega - \int_{\Gamma_t} \rho \bar{\mathbf{t}}^s \cdot \delta \mathbf{v} d\Gamma = 0, \quad (3)$$

where Ω is the material domain, Γ is the whole boundary, Γ_t is the boundary along which there exists prescribed tractions.

The continuum domain is described with a set of particles, so the mass density can be approximated as:

$$\rho(\mathbf{x}) = \sum_{p=1}^{n_p} m_p \delta(\mathbf{x} - \mathbf{x}_p), \quad (4)$$

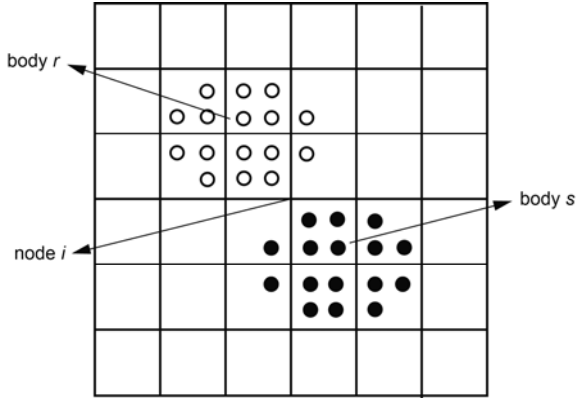


Figure 1 Material point discretization.

where m_p and x_p are the mass and the position of the particle p , and δ is the Dirac delta.

At each time step, the mass and velocities of the material particles are mapped onto the background cell using standard finite element shape functions. The mapped velocity \mathbf{v}_j of the node j is obtained through the following equation:

$$\sum_j m_{ij} \mathbf{v}_j = \sum_p m_p \mathbf{v}_p N_i(\mathbf{x}_p),$$

where N_i is the shape function of the background cell, m_{ij} is the consistent mass matrix which, for the sake of simplicity, is generally replaced with a lumped diagonal mass matrix $m_{ij} \delta_{ij}$. Accordingly, eq. (5) can be rewritten as:

$$m_i \mathbf{v}_i = \sum_p m_p \mathbf{v}_p N_i(\mathbf{x}_p), \quad (6)$$

where the lumped mass can be written as:

$$m_i = \sum_p m_p N_i(\mathbf{x}_p), \quad (7)$$

In this study, 8-point hexahedron element is used as the background grid and the shape function is given by

$$N_i = \frac{1}{8} (1 + \xi \xi_i) (1 + \eta \eta_i) (1 + \zeta \zeta_i), \quad (8)$$

where ξ , η and ζ are the natural coordinates of the material particle in the cell.

Taking eqs. (4), (6) and (7) into consideration, eq. (3) can be reduced to

$$\dot{\mathbf{p}}_i = \mathbf{f}_i^{\text{int}} + \mathbf{f}_i^{\text{ext}}, \quad (9)$$

where \mathbf{p}_i , $\mathbf{f}_i^{\text{int}}$ and $\mathbf{f}_i^{\text{ext}}$ are the respective momentum, internal force and external force vectors of node i , respectively. They are represented as:

$$\dot{\mathbf{p}}_i = \sum_p m_p N_i \mathbf{v}_p, \quad (10)$$

$$\mathbf{f}_i^{\text{int}} = - \sum_p \nabla N_i \cdot \boldsymbol{\sigma}_p \frac{m_p}{\rho_p}, \quad (11)$$

$$\mathbf{f}_i^{\text{ext}} = \sum_p m_p N_i \mathbf{b}_p + \mathbf{f}_i^{\text{con}}, \quad (12)$$

where $\mathbf{f}_i^{\text{con}}$ is the contact force at node i .

2.2 Contact algorithm

The treatment of most contact problems in FEM relies on the use of penalty functions and/or Lagrange multipliers. In the former, contact elements are used, while in the latter the contact stress is a by-product of the full assembled matrix. The difficulties associated with these approaches stem from the use of large penalty parameters that lead to ill-conditioning or the use of asymmetric sparse matrices in the case of Lagrange multipliers. This is readily overcome by the MPM. As a result of the single-valued mapping functions between background grid nodes and particles, interpenetration of material particles is precluded in the standard MPM algorithm. A no-slip contact constraint is inherent in the standard MPM. Since the column wall is under compression at all times during crushing, the no-slip contact can be used for the self-contact during progressive collapse and the formation of plastic folds without introducing significant errors. The contact method [22] is only applied between the column wall and the two rigid ends, so that the collapse load can be correctly simulated. The fundamental idea of the contact algorithm is given below.

As shown in Figure 1, the contact of the two bodies will be detected when the velocities are projected onto the same node:

$$(\mathbf{v}_i^r - \mathbf{v}_i^s) \cdot \mathbf{n}_i^r > 0, \quad (13)$$

where \mathbf{v}_i^r and \mathbf{v}_i^s are the velocity vectors of body r and s at node i , respectively. \mathbf{n}_i^r is the unit outward normal of body r at node i .

The contact force will be calculated and the velocities of the two bodies will be adjusted using the following expressions. The nodal velocity must satisfy the impenetrability condition, such that

$$\bar{\mathbf{v}}_i^r \mathbf{n}_i^r + \bar{\mathbf{v}}_i^s \mathbf{n}_i^s = 0, \quad (14)$$

where $\bar{\mathbf{v}}_i^r$ and $\bar{\mathbf{v}}_i^s$ are the adjusted nodal velocities, \mathbf{n}_i^s is the unit outward normal of body s at node i .

The contact force $\mathbf{f}_i^{\text{con}}$ applied to each body must obey Newton's third law, that is

$$\mathbf{f}_i^{\text{con},r} + \mathbf{f}_i^{\text{con},s} = 0, \quad (15)$$

where $\mathbf{f}_i^{\text{con},r}$ and $\mathbf{f}_i^{\text{con},s}$ are the contact node force of body r and body s , respectively. The contact force $\mathbf{f}_i^{\text{con}}$ can be divided into the normal part and tangential friction part.

In addition, the collinearity condition must be guaranteed at the contact surface, viz

$$\mathbf{n}_i^r + \mathbf{n}_i^s = 0. \quad (16)$$

For the modelling of column crushing, the correct unit outward normals of the flat plates can be calculated. Hence the unit outward normal of the column wall is set to be opposite to that of the plates.

Multiply eq. (14) with $m_i^r m_i^s$ and considering eq. (16), eq. (14) can be written as:

$$m_i^s \bar{\mathbf{p}}_i^r \cdot \mathbf{n}_i^r = m_i^r \bar{\mathbf{p}}_i^s \cdot \mathbf{n}_i^r, \quad (17)$$

where $\bar{\mathbf{p}}_i^r$ and $\bar{\mathbf{p}}_i^s$ are the updated nodal momenta of the contacting bodies. As the momentum is required to be unaltered, the updated nodal momenta are obtained

$$\bar{\mathbf{p}}_i^r = \mathbf{p}_i^r - \frac{m_i^s \mathbf{p}_i^r - m_i^r \mathbf{p}_i^s}{m_i^r + m_i^s} \cdot \mathbf{n}_i^r \mathbf{n}_i^r, \quad (18)$$

$$\bar{\mathbf{p}}_i^s = \mathbf{p}_i^s + \frac{m_i^s \mathbf{p}_i^r - m_i^r \mathbf{p}_i^s}{m_i^r + m_i^s} \cdot \mathbf{n}_i^r \mathbf{n}_i^r, \quad (19)$$

The unit surface normal vector is computed by the gradient of the nodal mass m_i^r of the individual body [23]:

$$\mathbf{n}_i^r = \frac{1}{\left| \sum_p \nabla N_i m_p^r \right|} \sum_p \nabla N_i m_p^r, \quad (20)$$

where m_p^r is the mass of particle p in body r . In this paper, tubes are compressed under the movement of plates. The contact normal vector is set to be consistent with the normal of the plates.

The nodal force is updated by

$$\bar{\mathbf{f}}_i = \mathbf{f}_i + \mathbf{f}_i^{\text{con}}. \quad (21)$$

The contact force is expressed as:

$$\mathbf{f}_i^{\text{con},r} = -\mathbf{f}_i^{\text{con},s} = -f_i^{\text{nor}} \mathbf{n}_i^r - f_i^{\text{fric}} \mathbf{s}_i^r, \quad (22)$$

where \mathbf{s}_i^r is the unit tangential at node i along the boundary. f_i^{nor} and f_i^{fric} are detailed as:

$$f_i^{\text{nor}} = \frac{m_i^s \mathbf{f}_i^{r,\text{int}} - m_i^r \mathbf{f}_i^{s,\text{int}}}{m_i^r + m_i^s} \cdot \mathbf{n}_i^r, \quad (23)$$

$$f_i^{\text{fric}} = \min(\mu f_i^{\text{nor}}, f_i^{\text{tan}}), \quad (24)$$

$$f_i^{\text{tan}} = \frac{(m_i^s \mathbf{p}_i^r - m_i^r \mathbf{p}_i^s + (m_i^s \mathbf{f}_i^{r,\text{int}} - m_i^r \mathbf{f}_i^{s,\text{int}}) \Delta t) \cdot \mathbf{s}_i^r}{(m_i^r + m_i^s) \Delta t}, \quad (25)$$

where μ is the coefficient of friction, Δt is the time step.

2.3 Explicit solver

The MPM explicit solver MPM3D [24–26] is used to simulate the column crushing. In our method, the leapfrog central difference method is employed to integrate eq. (9). The variable time step size Δt is calculated by

$$\Delta t = \frac{d_c}{\max(c + |\mathbf{v}_p|)}, \quad (26)$$

where d_c is the interval of the background cell, c is sound speed.

The superscript k indicates the value of variable at time t^k . The velocity of particles at time $t^{k+1/2}$ is updated as:

$$\mathbf{v}_p^{k+1/2} = \mathbf{v}_p^{k-1/2} + \sum_i \Delta \mathbf{p}_i^k N_i^k / m_i^k, \quad (27)$$

where

$$\Delta \mathbf{p}_i^k = (\mathbf{f}_i^{k,\text{int}} + \mathbf{f}_i^{k,\text{ext}}) \Delta t^k. \quad (28)$$

The position of particles at time t^{k+1} is given by

$$\mathbf{x}_p^{k+1} = \mathbf{x}_p^k + \Delta t^{k+1/2} \sum_i \mathbf{p}_i^{k+1/2} N_i^k / m_i^k, \quad (29)$$

where

$$\mathbf{p}_i^{k+1/2} = \mathbf{p}_i^{k-1/2} + \Delta \mathbf{p}_i^k. \quad (30)$$

It should be noted that $t^{k+1} = t^k + \Delta t^{k+1/2}$, $t^{k+1/2} = t^k + \Delta t^{k+1/2} / 2 = t^{k-1/2} + \Delta t^k$ and $\Delta t^k = (\Delta t^{k-1/2} + \Delta t^{k+1/2}) / 2$.

3 Material model and convergence tests

The accuracy of the MPM simulation is determined by the number of the particles and the size of the background cells. In this paper, the thin wall structures are directly modelled by particles. It is critical to carry out convergence tests to determine the minimum number of particles needed for the thickness of the wall so that MPM can capture the correct deformation modes of the columns. The results are compared with the experiments which were carried out by Johnson et al. [7].

In our model, the PVC column rests on a rigid support, and is struck by a rigid plate. The elastic-perfectly plastic constitutive law was adopted for the PVC from [7] with the following mechanical properties: elastic modulus $E=3378.4$ MPa, Poisson's ratio $\nu=0.42$, and yield stress $\sigma_y=65.5$ MPa [7]. The properties of the rigid support and rigid striker were taken to be 10,000 times that of the PVC. The PVC column was modelled using the same geometries tested in [7]; with the wall thickness $t=3.2$ mm, the mean diameter $d=22.2$ mm and the length $l=76.2$ mm. To correctly model the frictionless contact between the column and the rigid ends, the friction coefficient was set to be as small as 0.02.

In this simulation, the upper plate crushed the column at a constant travelling speed of 10 m/s. The load condition is actually the direct displacement control condition which is consistent with experimental results. The direct displacement control is commonly used in the experimental and numerical study of tube crush behaviour [12,14,27]. However the solution with the direct displacement control will not be able to represent the snap-back or snap-through phenomenon as studied by Chen and Schreyer [28]. In this paper, we focus on the deformation mode and mean collapse load.

Four cases involving different numbers of particles chosen to discretize the column were studied. Table 1 gives the discretization parameters for the convergence study. The thickness of the column was discretized into 2, 4, 6 and 8 particles, respectively. The interval of the background was set to be two times of the distance of adjacent particles. Furthermore, the dynamic grid scheme [26] was used to reduce the computational storage and improve the computations efficiency.

The final configurations of the column after axial crushing are compared against the experiment result, as given in Figure 2. Only two folds are formed in the case where only two particles are used in the thickness direction. With the increase of particle number to 6, three folds were obtained which were identical to the experiments of Johnson et al. [7]. It is determined that 6 particles are enough for discretizing the thickness of the column investigated here.

With the efficient contact method employed here, it is readily apparent to view the response of the tube under lateral loading. There is no additional shell algorithm applied for modelling the thin-walled structure. The convergence study of the tube under lateral loading is also presented here. The deformation mode of the tube under lateral compression is given in Figure 3. The deformed contour of the tube consists of four arcs whilst large plastic deformation occurs at the hinges.

4 Results and discussions

Figure 4 presents the axial load-displacement curves for the columns with different discretizing parameters. The response of load-displacement shows a distinct drop in the crush load whenever a fold is formed. The status change in contact of the adjacent structures of the column made some perturbation of the curve. The total energy absorbed (TEA) is presented by the area under the load-displacement curve is given as:

$$E = \int_0^U p(u)du, \tag{31}$$

where U is the total displacement, $p(u)$ is the function of the load curve. It is calculated by

$$E = \sum_{i=1}^n \frac{P_{i-1} + P_i}{2} \cdot \Delta u, \tag{32}$$

where n is the total number of displacement increments. Δu is the interval of the displacement. The mean collapse load \bar{P} is determined by equating TEA to the mean collapse load multiplied by the total displacement.

$$\bar{P} = \frac{E}{U}. \tag{33}$$

As to the six particles case, the mean crush load was found to be 13.2 kN. Based on a mean circumferential strain, Alexander [2] suggests the mean post-buckling load for

Table 1 Discretization parameters for the convergence study

Cases	Case (a)	Case (b)	Case (c)	Case (d)	Case (e)
Particles for the wall thickness	2	4	6	8	10
Total particles for the tube	4608	34944	112896	273408	527040

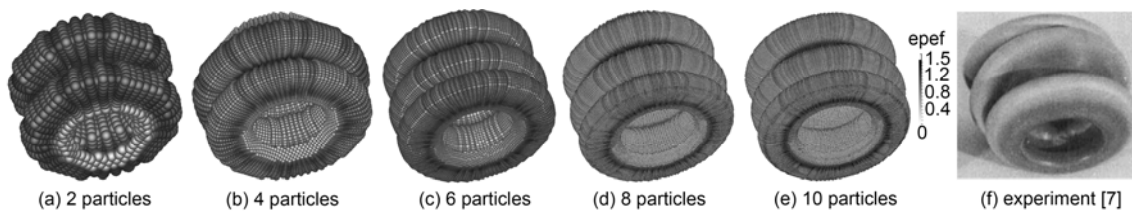


Figure 2 Deformation mode of the tube modelled by different numbers of particles in the thickness direction (axial loading).

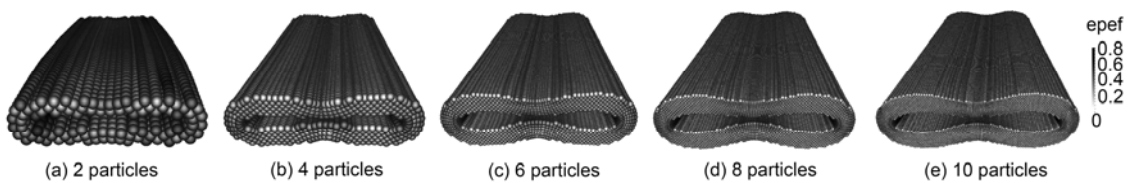


Figure 3 Deformation mode of the tube modelled by different numbers of particles in the thickness direction (lateral loading).

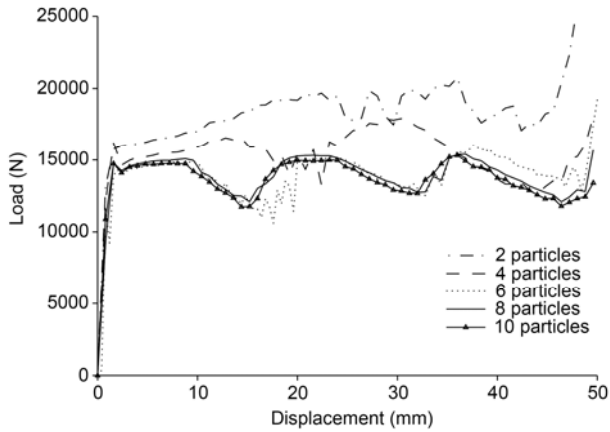


Figure 4 Load-displacement curve for the different discretization parameters.

metric ring buckling as being

$$\bar{P} = \pi t \sigma_y \sqrt{\frac{2\pi t d}{\sqrt{3}}}, \quad (34)$$

where σ_y is the yield strength. In this case, the theoretical mean post-buckling load can be calculated to be 10.5 kN. It is also noteworthy that although a small number of particles in the thickness direction results in fewer layers of lobes, the calculated mean collapse load does not show differ much as compared to the case where the number of particles was increased beyond 2.

As outlined earlier, MPM3D adopts explicit solver strategies in treating crashworthiness problems involving high-speed impact and explosive loading. To analyse quasi-static crush problems, the inertia effect should be insignificant. However, the impact speed of the striker should be above certain level to reduce the computational cost. In our case, the crush speed chosen was 10 m/s. Figure 5 compares the kinetic energy and the internal energy of the entire system of the 6 particles case. Compared to the internal energy of the tube, the kinetic energy can be considered negligible.

The force-displacement responses of the tubular columns under different impact velocities of 5, 10 and 15 m/s with 6 particles modelling of the thickness are presented in Figure 6. It is shown that the load-displacement responses are approximately the same in the three considered cases. This is because we adopted strain rate insensitive material model to simulate the behaviour of the PVC tubes. In addition, inertial stiffening effects are also negligible. In the following, the loading velocities are all set to be 10 m/s.

Figure 7 presents the lateral load-displacement curves for the columns with different discretizing parameters. The amount of plastic deformation in this mode is not as global as the axial crushing of tubes. Moreover, the mean load is lower than that in the axial loading case. A simple rigid plastic analysis for the lateral compression of a single tube was given by Deruntz and Hodge [29]. It was hypothesised

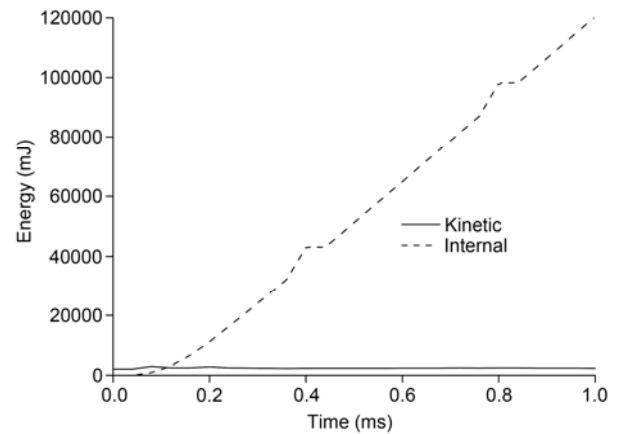


Figure 5 Comparison of the kinetic and internal energy of the tube.

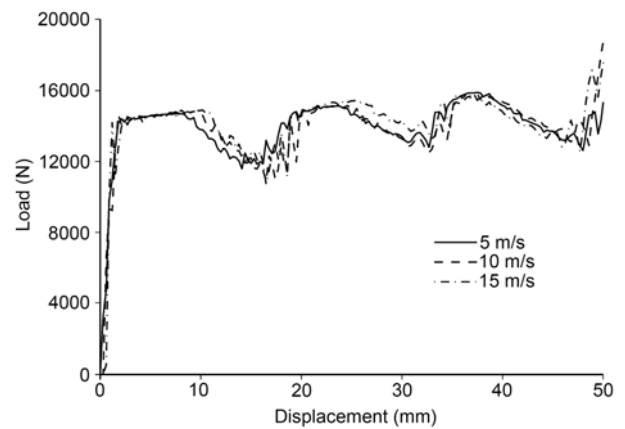


Figure 6 Load-displacement response for different velocities.

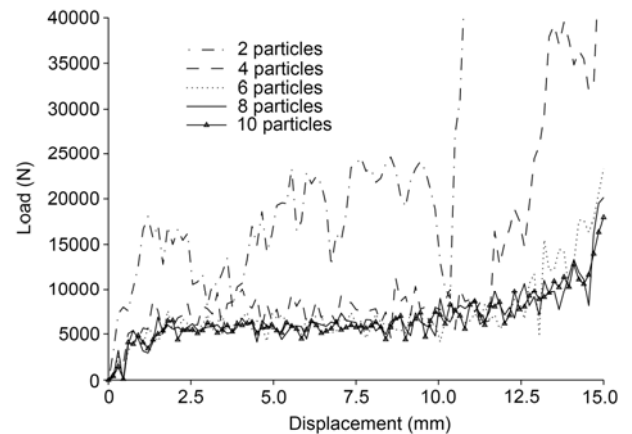


Figure 7 Load-displacement response for the case under lateral loading.

that the four circular arcs maintained their original radius and the plastic deformation only occurs at the hinges. However, the material strain hardening phenomena was negated. Accordingly the flattening force is given by

$$\bar{P} = \frac{4\sigma_y t^2 l}{\sqrt{3}d(1 - (\delta/d))^{1/2}}, \quad (35)$$

where δ is the deflection. Here $\delta=0$ and the theoretical flattening force is 5316.7 N, whilst the force of the 6 particle case in the simulation is 5763.4 N ($U=12.5$ mm).

As the elastic-perfectly plastic model is adopted in the simulation, the localized large plastic deformation might occur to incur the interaction between material and geometrical instabilities resulting in some oscillations in the load-displacement curves. It is observed that the oscillations are more obvious in the lateral loading case than the axial case. In the axial loading case, the folds are formed progressively. The plastic hinges travel from the top of tube to the bottom. The unfolded part still provides load support. As to the lateral loading case, the plastic deformation grows along the whole length of the tube as soon as the critical load is reached. As there is no hardening, the load oscillates around a certain level. The load begins to rise up until the top and bottom arcs get contacted with each other. However, since the evolution tendency of the load-displacement response and the computed mean collapse load are not distinctly affected by the oscillation, and thus no artificial damping is used to decrease the oscillations.

Figure 8 presents the computational cost with the increase of total number of particles (including the particles used for the plates). Both the axial and lateral loading case revealed a linear relation between the computational time and discretized particle number. It can be noted that the interval of the background cell is always set to be twice as the particle distance. Thus the computational cost of MPM3D just increases linearly with the decrease of discretization size.

4.1 Effect of selected trigger on accuracy of solution

To obtain the characteristic deformation modes, different triggers such as geometrical imperfections [12] and selected number of equidistant loading points [30] have been incorporated in former studies. Rust et al. [10] has demonstrated that the transient solution introduces oscillations per se is also a type of imperfection itself. It can be noted that the

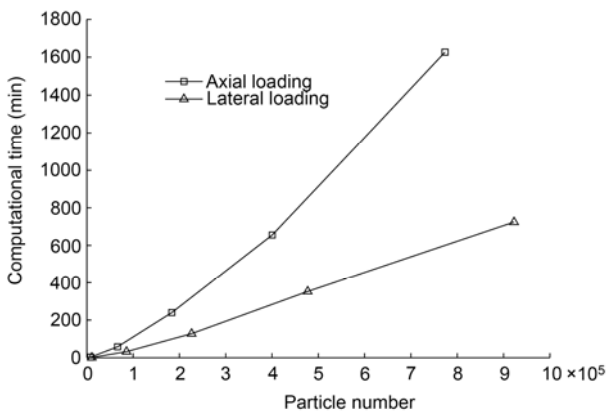


Figure 8 Growth of the computational time with the increase of particle number.

deformation mode obtained in sect. 0 can be attributed to the instability which could result from dynamic imperfections and particles discretization deviations.

In this section, a trigger based on material imperfection is implanted in MPM3D. This was achieved by randomly distributing some particle that can barely carry load. The percentage of the selected weak particles was limited to 0.3% to ensure that the total loading capacity of the column is not influenced. Following that, the effect of the random weak particles on the deformation mode is investigated.

Here we modelled two PVC columns with different wall thicknesses and mean diameters compared to that in section 0. The first case involves a column with $t=1.27$ mm and $d=20.32$ mm, while the second with $t=0.76$ mm and $d=19.81$ mm. The ratios of the wall thickness to the mean diameter t/d of the two cases are 0.063 and 0.038, respectively. The random distribution of weak particles in the first case is shown in Figure 9, where the red points represent the weak particles, as does the second case.

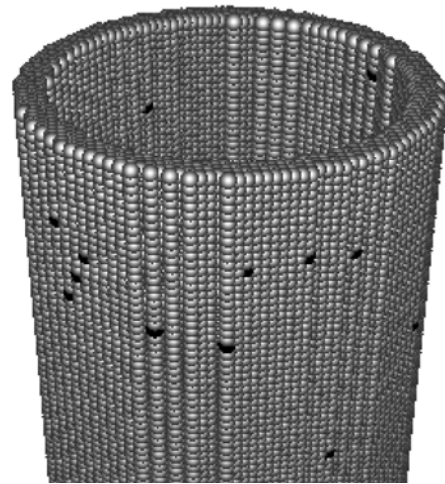


Figure 9 Random weak particles distribution of the tube with $t/d=0.063$.

In the simulation, four particles are used for the thickness of the first case, while three particles are used for the second case. Generally, fewer particles were needed for the thinner wall thickness. However, at least three particles were needed to ensure that there are more than one background cell along the wall thickness. The first fold layers of tubular columns modelled with the trigger and without are illustrated in Figure 10–13. Figures 10 and 11 depict the respective results of the first case from the top and side views, respectively. Figures 12 and 13 depict the result of second case. In the first case, it can be noted that without the randomly-distributed-weak-particles trigger the first fold develops as a ring mode. In the situation involving the trigger, the circumferential hinge which appeared at the first maximum load changed from a circular to a rectangular shape, which was identical to the experimental findings [7]. As time progresses, the hinges continued travelling and another

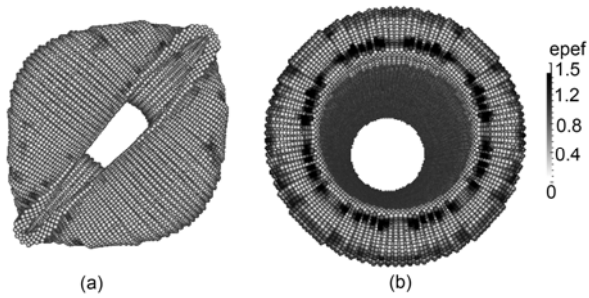


Figure 10 Predicted deformation modes of the tube with $t/d=0.063$ modelled (a) with and (b) without the trigger (top view).

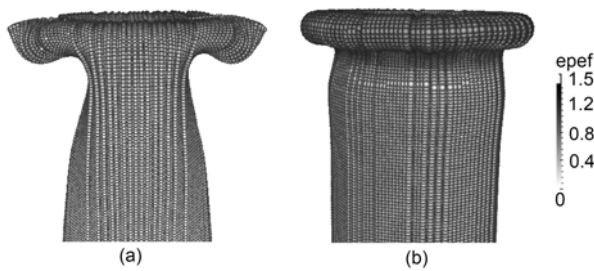


Figure 11 Predicted deformation modes of the tube with $t/d=0.063$ modelled (a) with and (b) without the trigger (side view).

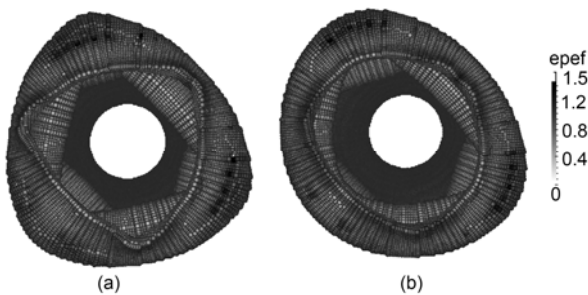


Figure 12 Predicted deformation modes of the tube with $t/d=0.038$ modelled (a) with and (b) without the trigger (top view).

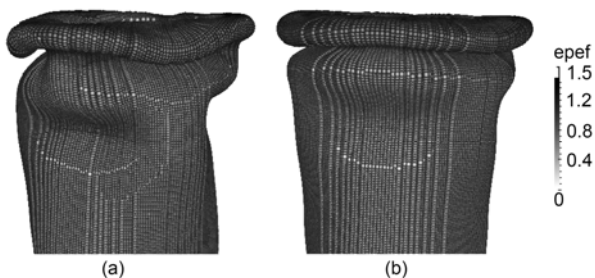


Figure 13 Predicted deformation modes of the tubes with $t/d=0.038$ modelled (a) with and (b) without the trigger (side view).

fold is formed. It can be noted again that the hinges became rectangular at a late stage in the situation without a trigger. Similar phenomenon is still observed in the second case. However, it is not as readily apparent as in the first case.

The trigger introduced here, accounting for the randomly weak property of the material, has an important role for the initiation and progression of the asymmetrical deformation modes.

4.2 Effect of normalized thickness/diameter ratio

Numerous research studies [3–9] have concluded that the deformation mode of a column under crushing will change from axisymmetric ring mode to non-axisymmetric diamond mode with the decreases of the ratio of the column thickness to diameter t/d . Our model has been validated for the axisymmetric ring mode in sect. 0, where t/d of the column is 0.143. For the columns with $t/d=0.063$ and $t/d=0.038$ in the previous subsection, the final configurations after crush are compared with the experimental results of Figures 14 and 15, respectively. It can be seen that with the help of the randomly-distributed-weak-particles trigger, both cases provide a realistic and detailed description of the deformation modes. The column with $t/d=0.063$ collapsed into to 2-lobe mode, while the column with $t/d=0.038$ collapsed into to 3-lobe mode.

The load-displacement curves of the two cases are provided in Figure 16. The first load peak is higher than the mean load for each case. This is because the initiation of buckling generally requires more energy input. The mean collapse load of the 2 and 3 lobes cases are calculated to be 2.7 and 1.0 kN, respectively.

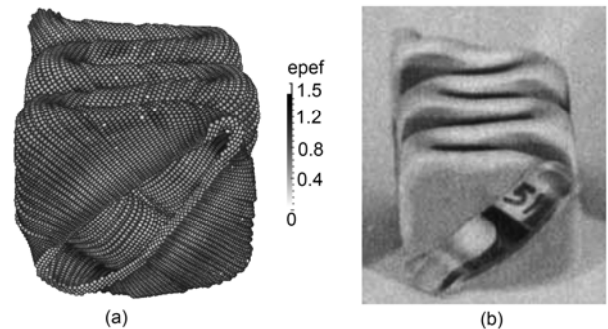


Figure 14 Comparison of (a) the model predictions with (b) the experimental findings of ref. [7] ($t/d=0.063$).

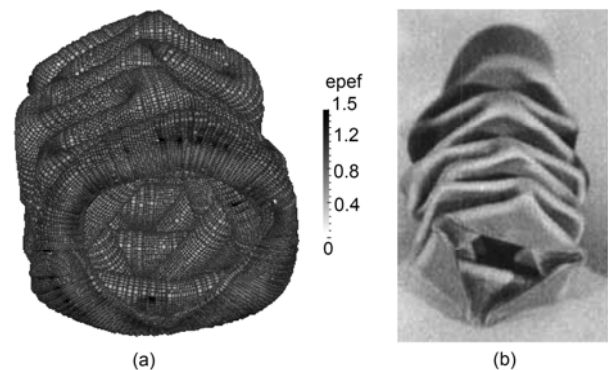


Figure 15 Comparison of (a) the model predictions with (b) the experimental findings of ref. [7] ($t/d=0.038$).

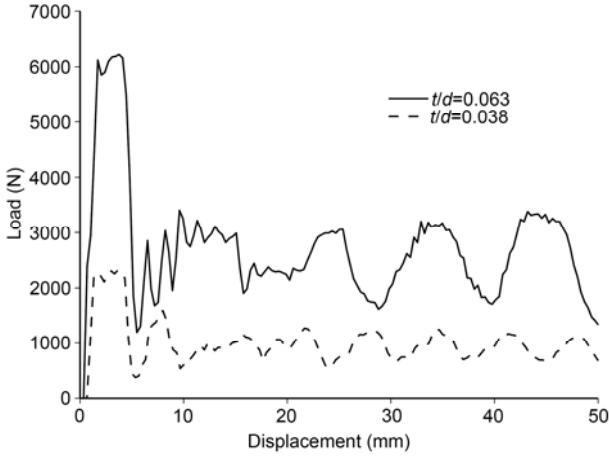


Figure 16 Load-displacement history of the tubes with different t/d .

Based on the travelling hinges concept, a non-dimensional analytical solution of the mean post-buckling stress was proposed by Johnson et al. [7] as:

$$\frac{\bar{\sigma}}{\sigma_y} = \frac{1}{\sqrt{3}} \frac{t}{D} \left[1 + n \operatorname{cosec}\left(\frac{\pi}{2n}\right) + n \cot\left(\frac{\pi}{2n}\right) + \frac{D}{r} \right], \quad (36)$$

where n is the number of the circumferential lobes and r is the radius of the travelling hinge. Some assumptions of that the radius of the travelling hinge remains constant and the column material always approaches the travelling hinge in a vertical direction were incorporated to simplify the calculation of r . Thus r could be replaced by r^* as:

$$r^* = \frac{D}{A} \left(\sqrt{1 + \frac{A}{2} \frac{\pi}{2n} \tan(\pi/2n)} - 1 \right), \quad (37)$$

where $A = 1 + n \operatorname{cosec}(\pi/2n) + n \cot(\pi/2n)$. For the first case, $n=2$ mode, the mean post-buckling stress could be derived as 32.1 MPa corresponding to a mean collapse load of 2.6 kN.

However, the analytical expression cannot be regarded as completely satisfactory according to the experimental results [7]. For the case where $n=3$ mode, eq. (38) which takes into consideration all the stationary hinges but ignores the travelling hinges, adequately describes the experimental results as follows:

$$\frac{\bar{\sigma}}{\sigma_y} = \frac{1}{\sqrt{3}} \frac{t}{D} \left[1 + n \operatorname{cosec}\left(\frac{\pi}{2n}\right) + n \cot\left(\frac{\pi}{2n}\right) \right], \quad (38)$$

Thus the mean collapse load is 0.84 kN.

It is shown that the simulation results in good agreement to the analytical solution, which has been validated by experimental findings. The mean collapse loads calculated by MPM modelling are somewhat higher than the analytical results. Comparing the two cases with that described in Section 0, our model demonstrated that the deformation mode

would shift from continuous axisymmetric ring mode to non-axisymmetric diamond mode with the decrease of t/d . The lobe number of diamond fold also depends on t/d . Columns with smaller size of t/d will be crushed into diamond folds with more lobes. Moreover, the mean collapse stress level of the column wall decreased with t/d .

4.3 Effect of normalized length/diameter ratio

Earlier work established the fact that the ratio of the length to the diameter l/d also has an important role on the collapse mode. Andrews et al. [8] specifically discussed the influence of the column length on the axial crushing modes and energy absorption properties. They found that aluminium columns with large ratio of l/d followed Euler's mode of buckling. It is only reasonable to assume that the PVC columns with larger l/d also possess similar feature. Based on the former correct modelling, we extend MPM simulation to predict the collapse modes of PVC columns with changing l/d parameters.

Compared to the first case in sect. 4.2, the columns studied here are different with diameters of $d=14, 12$ and 10 mm, corresponding to $l/d=5.4, 6.4$ and 7.6 , respectively. Randomly distributed weak particles were also selected to examine their effect on the collapse mode. Figure 17–19 depict the collapse modes of the columns. In the case of $l/d=5.4$, the first two folds were both symmetric rings without using the trigger while the second fold of the column turned out to be asymmetric when using the trigger. As to the smallest diameter $l/d=7.6$, the case with and without trigger resulted in the same Euler-buckling mode. This implies that the effect of the random weak particles is unnoticeable. It can be seen that the deformation of the column transformed from progressively inextensional mode to Euler-buckling mode as the l/d increases.

Figure 20 compares the load-displacement response of the three tubes with different l/d . The results are only shown for cases with the randomly-distributed-weak-particles trigger. The tube becomes stronger with the decrease of l/d . When $d=10$ mm ($l/d=7.6$), the load drops after reaching a certain peak. The local plastic deformation and non-repeatable collapse mode resulted in low energy absorption. In practice, this type of thin tubular column should be avoided for cases requiring energy absorption.

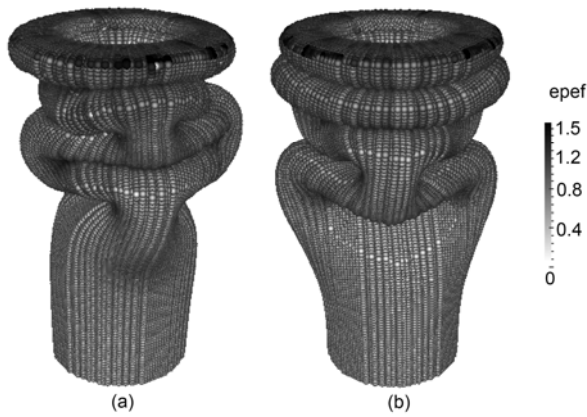


Figure 17 Deformation mode for the tube with $l/d=5.4$ modelled (a) with and (b) without random weak particles.

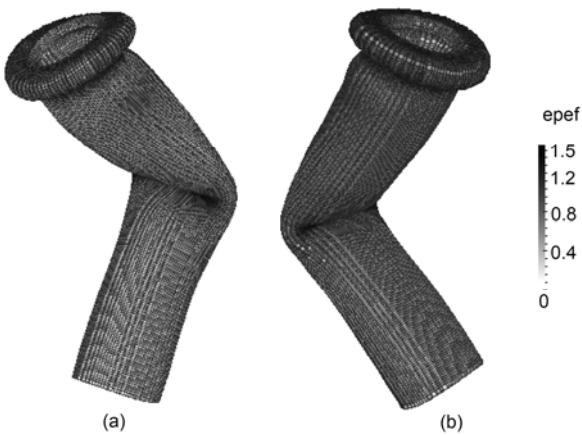


Figure 18 Deformation mode for the tube with $l/d=6.4$ modelled (a) with and (b) without random weak particles.

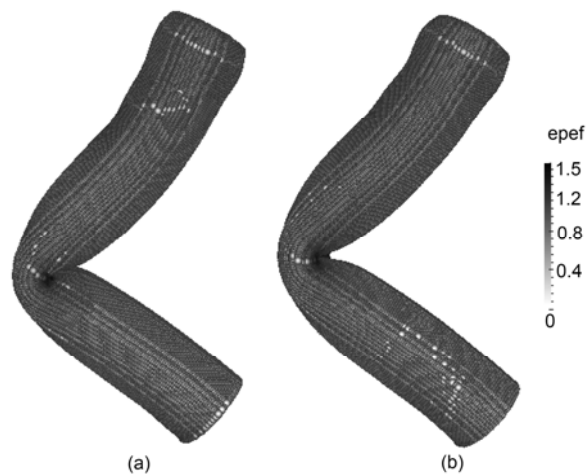


Figure 19 Deformation mode for the tube with $l/d=7.6$ modelled (a) with and (b) without random weak particles.

5 Conclusions

In this paper, the material point method is adopted to accu-

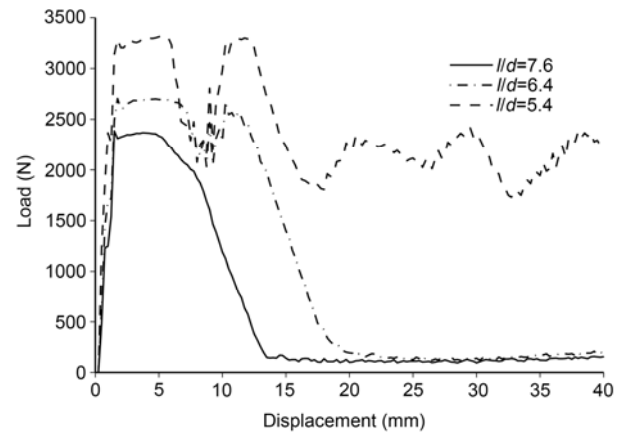


Figure 20 Predicted load-displacement response of the tubes with different l/d .

ately model the crush behaviour of PVC tubular columns. A direct three dimensional particle discretization is implemented to capture the detailed progressive collapse patterns, the associated crippling load history and mean collapse loads. The presented model is validated by comparison with earlier experiments and the results show good agreement between the model predictions and the experimental findings. Furthermore, our work shows that introducing randomly-distributed-weak-particles triggers enabled us to capture the non-axisymmetric deformation modes accurately. Interestingly, our model predicts that the deformation modes of the tubular columns change from the continuous ring modes to the diamond ones as the ratio of the wall thickness to the diameter t/d increases. It also predicts that columns with smaller t/d tend to form more lobes. The work was further extended to examine the effect increased l/d upon the resulting buckling mode. Specifically, for the case where $l/d < 7.6$, the collapse mode was progressive and beyond this ratio, the tube followed Euler-type buckling mode.

This work was supported by the National Basic Research Program of China (Grant No. 2010CB832701) and Natural Sciences and Engineering Research Council of Canada (NSERC).

- 1 Mallock A. Note on the instability of tubes subjected to end pressure and on the folds in a flexible material. Proc R Soc Ser A, 1908, 81: 388–393
- 2 Alexander J M. An approximate analysis of thin cylindrical shells under axial loading. Q J Mech Appl Math, 1960, 13: 10–15
- 3 Pugsley A, Macaulay M. The large scale crumpling of thin cylindrical columns. Q J Mech Appl Math, 1960, 13: 1–9
- 4 Pugsley A. On the crumpling of thin tubular struts. Q J Mech Appl Math, 1979, 32(1): 1–7
- 5 Abramowicz W, Jones N. Dynamic axial crushing of circular tubes. Int J Impact Eng, 1984, 2: 263–281
- 6 Abramowicz W, Jones N. Dynamic progressive buckling of circular and square tubes. Int J Impact Eng, 1986, 4: 243–269
- 7 Johnson W, Soden P D, Al-Hassani S T S. Inextensional collapse of thin-walled tubes under axial compression. J Strain Anal Eng Des,

- 1977, 12: 317–330
- 8 Andrews K R F, England G L, Ghani E. Classification of the axial collapse of cylindrical tubes under quasi-static loading. *Int J Mech Sci*, 1983, 25(9-10): 687–696
 - 9 Singace A A, El-Sobky H. Interplay of factors influencing collapse modes in axially crushed tubes. *Int J Crashworthiness*, 2000, 5(3): 279–298
 - 10 Rust W, Schweizerhof K. Finite element limit load analysis of thin-walled structures by ANSYS (implicit), LS-DYNA (explicit) and in combination. *Thin Wall Struct*, 2003, 41: 227–244
 - 11 Marzbanrad J, Abdollahpoor A, Mashadi B. Effects of the triggering of circular aluminum tubes on crashworthiness. *Int J Crashworthiness*, 2009, 14(6): 591–599
 - 12 Meguid S A, Stranart J C, Heyerman J. On the layered micromechanical three-dimensional finite element modelling of foam-filled columns. *Finite Elem Anal Des*, 2004, 40: 1035–1057
 - 13 Meguid S A, Attia M S, Stranart J C, et al. Solution stability in the dynamic collapse of square aluminium columns. *Int J Impact Eng*, 2007, 34: 348–359
 - 14 Zhang X, Cheng G D, You Z, et al. Energy absorption of axially compressed thin-walled square tubes with patterns. *Thin Wall Struct*, 2007, 45: 737–746
 - 15 Younes M M. Finite element modeling of crushing behaviour of thin tubes with various cross-sections. In: 13th International Conference on aerospace sciences & aviation technology, Egypt, 2009
 - 16 Fyllingen Ø, Hopperstad O S, Hanssen A G, et al. Modelling of tubes subjected to axial crushing. *Thin Wall Struct*, 2010, 48: 134–142
 - 17 Noguchi H, Kawashima T, Miyamura T. Element free analysis of shell and spatial structures. *Int J Numer Meth Eng*, 2000, 47: 1215–240
 - 18 Li S, Hao W, Liu W K. Numerical simulations of large deformation of thin shell structures using meshfree methods. *Comput Mech*, 2000, 25: 102–116
 - 19 Gato C. Meshfree analysis of dynamic fracture in thin-walled structures. *Thin Wall Struct*, 2010, 48: 215–222
 - 20 Ma S, Zhang X, Qiu X M. Comparison study of MPM and SPH in modeling hypervelocity impact problems. *Int J Impact Eng*, 2009, 36: 272–282
 - 21 Sulsky D, Chen Z, Schreyer H L. A particle method for history-dependent materials. *Comput Method Appl Mech*, 1994, 118: 179–196
 - 22 Huang P, Zhang X, Ma S. Contact algorithms for the material point method in impact and penetration simulation. *Int J Numer Meth Eng*, 2011, 85(4): 498–517
 - 23 Bardenhagen S G, Guilkey J E, Roessig K M, et al. An improved contact algorithm for the material point method and application to stress propagation in granular material. *CMES-Comput Modeling Eng*, 2001, 2(4): 509–522
 - 24 Zhang Y T, Zhang X, Liu Y. An alternated grid updating parallel algorithm for material point method using OpenMP. *CMES-Comput Modeling Eng*, 2010, 69(2): 143–165
 - 25 Lian Y P, Zhang X, Liu Y. Coupling of finite element method with material point method by local multi-mesh contact method. *Comput Method Appl Mech*, 2011, 200: 3482–3494
 - 26 Ma Z T, Zhang X, Huang P. An object-oriented mpm framework for simulation of large deformation and contact of numerous grains. *CMES-Comput Modeling Eng*, 2010, 51(1): 61–87
 - 27 Bardi F C, Yun H D, Kyriakides S. On the axisymmetric progressive crushing of circular tubes under axial compression. *Int J Solids Struct*, 2003, 40: 3137–3155
 - 28 Chen Z, Schreyer H L. Secant structural solution strategies under element constraint for incremental damage. *Comput Method Appl Mech*, 1991(90): 869–884
 - 29 Deruntz J A, Hodge P G. Crushing of a tube between rigid plates. *J Appl Mech*, 1963, 30: 391–396
 - 30 Galib D A, Limam A. Experimental and numerical investigation of static and dynamic axial crushing of circular aluminum tubes. *Thin Wall Struct*, 2004, 42: 1103–1137